# Electrochemical Reduction of Dissolved Oxygen in Alkaline, Solid Polymer Electrolyte Films

David Novitski,[†] Aslan Kosakian,[‡] Thomas Weissbach,[†] Marc Secanell,[‡] and Steven Holdcroft*,[†]

[†]Department of Chemistry, Simon Fraser University, Burnaby, British Columbia V5A 1S6, Canada
[‡]Department of Mechanical Engineering, University of Alberta, Edmonton, Alberta T6G 1H9, Canada

S *Supporting Information*
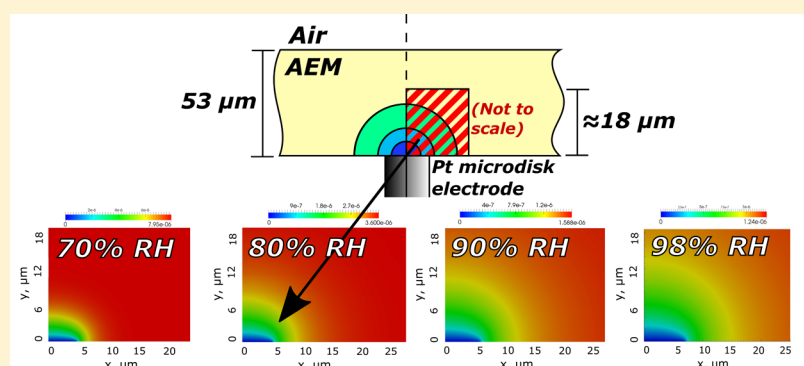
ABSTRACT: Mass transport of oxygen through an ionomer contained within the cathode catalyst layer in an anion exchange membrane fuel cell is critical for a functioning fuel cell, yet is relatively unexplored. Moreover, because water is a reactant in the oxygen reduction reaction (ORR) in alkaline media, an adequate supply of water is required. In this work, ORR mass transport behavior is reported for methylated hexamethyl-*p*-terphenyl polymethylbenzimidazoles (HMT-PMBI), charge balanced by hydroxide ions (IEC from 2.1 to 2.5 mequiv/g), and commercial Fumatec FAA-3 membranes. Electrochemical mass transport parameters are determined by potential step chronoamperometry using a Pt microdisk solid-state electrochemical cell, in air at 60 °C, with relative humidity controlled between 70% and 98%. The oxygen diffusion coefficient (D_{bO2}), oxygen concentration (c_{bO2}), and oxygen permeability ($D_{bO2} \cdot c_{bO2}$) were obtained by nonlinear curve fitting of the current transients using the Shoup–Szabo equation. Mass transport parameters are correlated to water content of the ionomer membrane. It is found that the oxygen diffusion coefficients decreased by 2 orders of magnitude upon reducing the water content of the ionomer membrane by lowering the relative humidity. The limitation of the Shoup–Szabo equation for extracting ORR mass transport parameters using thin ionomer films was evaluated by numerical modeling of the current transients, which revealed that a significant discrepancy (up to 29% under present conditions) was evident for highly hydrated membranes for which the oxygen diffusion coefficient was largest, and in which the oxygen depletion region reached the ionomer/gas interface during the chronoamperometric analysis.

■ INTRODUCTION

Anion exchange membranes (AEMs) for use in alkaline anion exchange membrane fuel cells (AAEMFCs) rely on the transport of hydroxide ions. Benefits of AAEMFCs, over traditional proton exchange membrane (PEM) fuel cells, include the prospect of eliminating noble-metal-based catalysts.[1−3] Several approaches to designing AEMs having hydroxide ion stability have been explored, and include membranes based on polymers bearing cationic tetraalkylammonium,[4] phosphonium,[5] DABCO,[6] and imidazolium head groups.[7] Recently, we reported the synthesis of hexamethyl-*p*-terphenyl poly(methylbenzimidazolium) (HMT-PMBI), schematically shown in Figure 1A. In this ionic polymer, the backbone serves as both the hydrophobic and hydrophilic component. Steric hindrance provided by the hexamethyl-*p*-terphenyl (HMT) group alleviates a major degradation pathway, ring opening, caused by hydroxide attack on the C2

position of the benzimidazolium group.[8,9] The precursor polymer can be controllably methylated to increasing extents to provide ionomers with varying ion exchange capacity (IEC). A polymer with 89% degree of methylation (which corresponds to an ion exchange capacity of 2.5 mequiv/g) is alcohol or water−alcohol soluble, water insoluble, and exhibits a hydroxide conductivity of 17.3 mS/cm at 95% RH and 90 °C.[10] HMT-PMBI-OH⁻ exhibits a high resistance to hydroxide attack: only 6% loss of functional groups after 7 days in 2 M NaOH at 80 °C.[10−12]

In basic media, the 4-e⁻ oxygen reduction reaction (ORR) occurs according to the following equation:

$$O_2 + 2H_2O + 4e^- \rightarrow 4OH^- \tag{1}$$
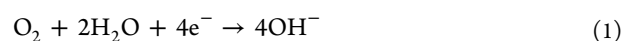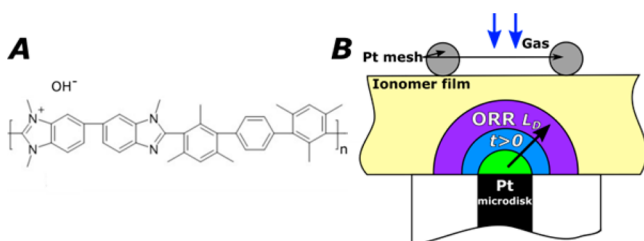
Figure 1. (A) Greater than 50% methylation of HMT-PMBI results in HMT-PMBI-OH⁻. The IEC is controlled by the degree of methylation (50% methylation corresponds to 0 mequiv/g, 100% methylation corresponds to 3.14 mequiv/g). (B) Illustration of the oxygen depletion region (where L_D is diffusion length) in an ionomer film at a Pt microdisk electrode during ORR. The Pt mesh serves as the counter electrode, and allows for gas exchange directly above the platinum microdisk.

In the case of catalyst layers in AAEMFCs, a thin hydroxide-conducting ionomer is employed to provide hydroxide ion conductivity, and to provide the basic media for the reaction in the cathode catalyst layer. Oxygen must diffuse into, and transport through, the ionomer film in order to reach catalyst sites and participate in the ORR. Ingress of water into the ionomer is also critical because water is a reactant in the ORR.

Oxygen mass transport in hydroxide conducting ionomers has thus far been sparsely investigated, and the reports that are available use highly humidified or liquid water hydrated conditions.[13,14] For example, under fully humidified inlet gas streams, oxygen gas permeabilities were observed for a commercially available quaternary ammonium-based AEM (Tokuyama A201, Tokuyama Corp., Tsukuba, Japan) in OH⁻ form (3.99×10^{-12} mol/cm·s).[14] The permeabilities (which are similar to Nafion 211) were attributed to a high oxygen diffusion coefficient in the AEM. Using a hydroxide conducting ionomer (AS-4 ionomer solution, Tokuyama Corp., Tsukuba, Japan) cast on a rotating disk electrode, another study reported an oxygen permeability coefficient of 4.99×10^{-12} mol/(cm·s) in 0.1 M KOH.[13] The same group suggested that mass transport losses observed in an operating fuel cell were attributed to loss of water at the cathode catalyst layer rather than poor oxygen permeability.[15]

Solid-state electrochemical techniques using microdisk electrodes to study ORR have been used to elucidate oxygen mass transport coefficients in PEM materials over a wide range of environmental conditions. It is observed that an increase in temperature, pressure, or IEC ordinarily results in larger oxygen diffusion and permeability coefficients in both perfluorinated and hydrocarbon-based polymers.[16−22] In this report, we apply solid-state electrochemical methods, namely chronoamperometry, to study ORR in HMT-PMBI-OH⁻ films cast from methanol solutions. A comparison of the HMT-PMBI-OH⁻ ORR mass transport coefficients is made with respect to a commercially available AEM obtained from FuMA-Tech GmbH, FAA-3, which is a quaternary ammonium-based hydroxide polymer that has been successfully characterized in complete AAEMFC systems.[23,24]

The current transients that result from chronoamperometry were analyzed using the Shoup−Szabo equation to ascertain mass transport coefficients. To investigate the limitations of the Shoup−Szabo equation for the case of thin films deposited on working electrodes, a numerical model was also developed which accounted for the expanding oxygen depletion region in the films (Figure 1B). Characteristic changes in electrochemi-

cally active surface area (ECSA) and oxygen mass transport coefficients are reported for HMT-PMBI-OH⁻ possessing 3 values of IEC, and for FAA-3 membranes, at 60 °C in air. The relative humidity was lowered from near-saturated conditions (98% RH) to 70%, which adds a higher level of complexity to the measurements due to lower water content of the film and an increase in ionic resistance. By reducing the RH, the dependence of ORR on the level of hydration was examined. These data are discussed and compared in the context of varying the IEC, with respect to commercial AEM materials, and with respect to PEM materials, where more is known about ORR mass transport.

■ EXPERIMENTAL SECTION

A description of the preparation of the polymers investigated, the characterization methods, including the solid-state electrochemical cell (Figure S2) and the foundation of the numerical model are described in the Supporting Information. Briefly below, we describe the method used for obtaining oxygen mass transport limiting current transients and their analysis. Electrochemical potentials are reported versus a Pt pseudoreference electrode, as previously described, which was determined to be approximately −0.875 V vs the dynamic hydrogen electrode.[25]

Chronoamperometric, Potential Step Measurements. Chronoamperometry of the ORR was performed by holding the working electrode at a potential where no Faradaic reaction occurs (+0.2 V vs Pt), and switching to a potential where ORR is mass transport limited (e.g., −0.5 V vs Pt) at an acquisition rate of 400 data points per second within a current range of 10 nA. The mass transport limiting potential region for ORR was determined by linear sweep voltammetry between +0.2 and −0.5 V vs Pt using a scan rate of 150 mV/s. Current transient responses from the ORR mass transport limiting region were reproducible, and the averaged current transient was analyzed using the Shoup−Szabo equation (eq 2) which describes the current transient at microdisk electrodes:[26]

$$f(\tau) = 0.7854 + 0.8862\tau^{-1/2} + 0.2146\exp(-0.7823\tau^{-1/2}) \tag{2}$$

where $\tau = \frac{4D_{bO2}t}{r^2}$, $f(\tau) = \frac{i}{i_{ss}}$, $i_{ss} = 4nFD_{bO2}c_{bO2}r$, n is the number of electrons transferred in the reaction (4 for ORR on Pt), F is Faraday's constant (96 485 C/mol), D_{bO2} is the O₂ diffusion coefficient (cm²/s), c_{bO2} is the O₂ solubility (mol/cm³), t is time (s), and r is the radius of the microdisk (cm).[27] Equation 2 is reported accurate to 0.6% for all experimental time samplings.[26] Nonlinear curve fitting was performed using MATLAB software. The MATLAB script used to fit the current transients required truncation of several initial data points in order to eliminate contributions of non-Faradaic (double layer) charging. This step was performed as it is generally considered to be good practice to disregard at least the first 5 cell time constants, $R_u \cdot C_d$, (where R_u is uncompensated resistance and C_d is double-layer capacitance), in order to assume an instant change in interfacial oxygen concentration at the adjusted $t = 0$ s (non-Faradaic charging complete).[28] In this work, a time truncation of $\cong 0.2$ s was sufficient.[29] The MATLAB script includes time shifting in the fitting, so as to account dynamically for the non-Faradaic charging removed during truncation, and sets the initial point of the truncated data at $t = t_{trunc} - t_{shift}$ in order to provide a reliable fit that removes all temporal electrochemical effects.
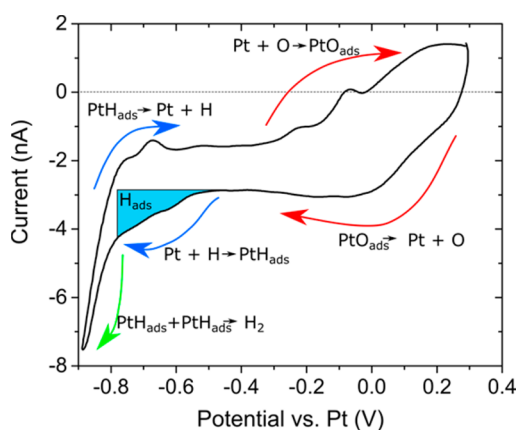
■ RESULTS

Water Uptake and λ. As the water content of ionomer films was expected to influence ORR parameters, water uptake was measured and the number of water molecules per ion exchange site (λ) as a function of RH were calculated (shown in Figure 2). Both water uptake and λ increase linearly from 20% to 75% RH. At 75% RH, 6 water molecules are present for each ion exchange site. At RH higher than 75%, λ increases
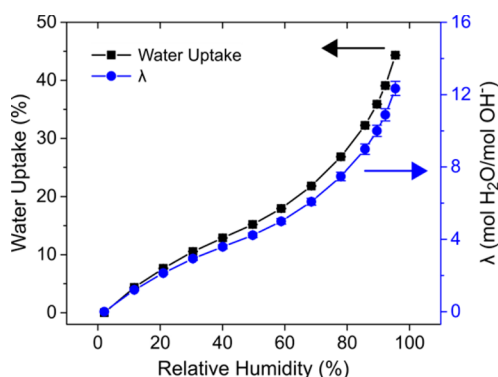
Figure 2. Water uptake and water molecules per ion exchange site (λ) of 2.5 mequiv/g HMT-PMBI-OH⁻ as a function of RH at 60 °C. Film thickness = 81 ± 3 μm.

exponentially, reaching a value of 12 at 95% RH. λ values for HMT-PMBI-OH⁻ (2.5 mequiv/g IEC) are similar to those reported for Nafion 211 under similar conditions.[30]

Electrochemically Active Surface Area. A representative cyclic voltammogram (CV) obtained for HMT-PMBI-OH⁻ (IEC 2.5 mequiv/g) at 60 °C, 90% RH is shown in Figure 3.


Figure 3. Cyclic voltammogram for 2.5 mequiv/g HMT-PMBI-OH⁻ at 90% RH and 60 °C, with scan rate of 250 mV/s. The pseudoreference electrode is Pt.[25]

The cathodic current bias results from the presence of oxygen in the environmental chamber. Representative CV's for other hydroxide conducting ionomer films are shown in Figure S3. As can be seen in Figure 3, sweeping the applied potential to values more negative than the initial +0.3 V versus the pseudo-Pt reference electrode gives rise to a peak that is due to the reduction of platinum oxide (−0.06 V), followed by cathodic current due to hydrogen adsorption which onsets at −0.5 V, and hydrogen evolution which onsets at −0.8 V. On the reverse potential sweep, anodic current due to hydrogen desorption onsets at −0.77 V, followed by platinum oxide formation which onsets at −0.26 V. The CV indicates that the ORR is occurring at the Pt electrode and that the ionomer is supporting ORR, i.e., it does not poison the catalyst.

Lindström et al. observed a marked decrease in the ECSA of carbon supported Pt catalyst in a membrane electrode assembly when the RH was decreased.[31] The lower ECSA was attributed to an increase of hydrophobic character at the ionomer−electrode interface blocking access to the Pt surface. A similar behavior has been revealed through conductive atomic force

microscopy, where the interfacial conductive area drastically dropped from ~95% active area at 84% RH to 4.1% at 30% RH for Nafion 212 membrane.[32] To determine whether a similar interfacial inversion occurs in anion exchange ionomers, the ECSA of the Pt microdisk electrode was calculated from cyclic voltammograms at 60 °C under different conditions of RH by integrating the charge due to hydrogen adsorption after correcting for double-layer charging. The potential range for hydrogen underpotential deposition (H_{UPD}) was chosen by correcting for the potential shift for the Pt pseudoreference (−0.875 V vs NHE). As the potential region for H_{UPD} vs NHE typically occurs between +0.1 and +0.4 V vs NHE, the potential range of −0.77 and −0.5 V (vs Pt) was used. Khadke and Krewer calculated the ECSA for Pt/C coated particles with a thin film of anion exchange ionomer (AS-4, Tokuyama) in 0.1 M KOH by averaging the charges for the H_{ads} and H_{des} peaks.[13] In the present investigation, only the H_{ads} peak is used for ECSA determination because the H_{ads} and H_{des} peaks are distorted cathodically by the early onset of the H_2 evolution peak, caused at low RH and on polycrystalline electrodes, a limitation of the solid-state electrochemical setup.[31]

The calculated ECSA values are shown in Figure 4, wherein the dashed line represents the geometric surface area of the
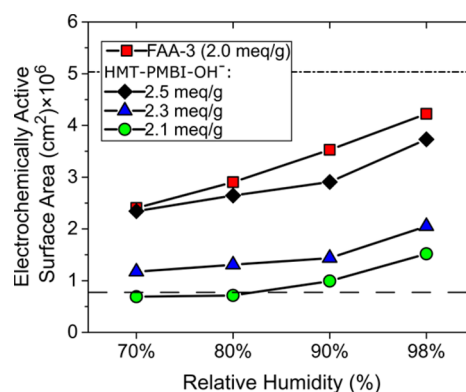

Figure 4. Calculated effective working electrode surface area at 60 °C. Dashed line (− −) indicates the geometric surface area, 7.85×10^{-7} cm², whereas double dash-dash (−·−) line represents the maximum effective surface area of the electrode in 1 M KOH, 5.05×10^{-6} cm².

working electrode. The effective surface areas obtained are higher than the geometric area due to surface roughness, which is typically >2 for polycrystalline platinum but lower than the ECSA determined in aqueous KOH (1 M).[19] As RH is lowered, a decrease in the electrochemically active surface area is observed for all thin films studied, which is attributed to a collapse of ionically conductive domains at the electrode interface with decreasing water content. A similar decrease in ECSA with a reduction in RH has been observed in perfluorinated proton exchange polymers.[25] The IEC of the HMT-PMBI-OH⁻ samples affects the ECSA, whereas a higher IEC, and therefore higher water content, results in a higher ECSA throughout the RH values investigated. FAA-3 membrane, with an IEC of 2.0 mequiv/g, on the other hand, exhibited an ECSA higher than the 2.5 mequiv/g HMT-PMBI-OH⁻ film, suggesting different ionic channel characteristics between the two polymers. As a point of context, we note that at 70% RH, the electrochemically active surface area of the films decrease to approximately half their original surface area at 98% RH for all samples investigated, which is similar to the

conducting active area observed for Nafion 212 membrane at 70% RH.[32] The effective ECSA for the working electrode was used to determine an effective radius, r_{eff}, in the calculation of D_{bO2} and c_{bO2} (r_{eff} was computed using $\pi r_{eff}^2 = ECSA_{eff}$). The use of r_{eff} instead of the geometric radius is justified based on previously reported results.[25]

Potential Step Chronoamperometry. The initial and final applied potential values used for potential step chronoamperometry were based on linear sweep voltammograms (voltammograms are shown in Figure S4). From these, the initial potential of +0.2 V vs Pt was used and the final potential ranged from −0.4 to −0.5 V vs Pt as this region was well within ORR mass transport limiting conditions. The chronoamperometric current transients obtained by stepping from +0.2 to −0.4 V and from +0.2 to −0.5 V were averaged, with a maximum error obtained from range-normalized root-mean-square deviation (NRMSD, eq 3) between averaged and original experimental transients of 3.9% for 2.3 mequiv/g IEC HMT-PMBI-OH⁻ at 98% RH (1% average deviation across the other samples). Representative current transients for 2.5 mequiv/g IEC HMT-PMBI-OH⁻ at 60 °C and under RH between 70 to 98% are shown in Figure 5, together with least-
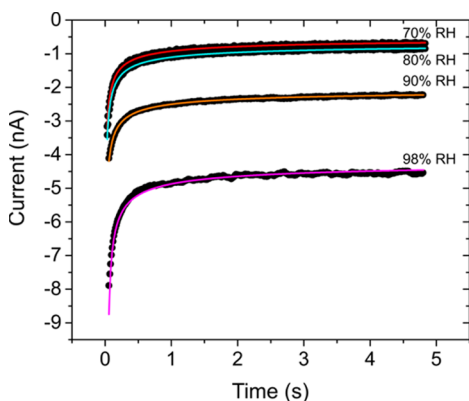

Figure 5. ORR current transients for HMT-PMBI-OH⁻ 2.5 mequiv/g at 60 °C in air. Least-squares fit solutions for the Shoup−Szabo equation are overlaid as fitted curves.
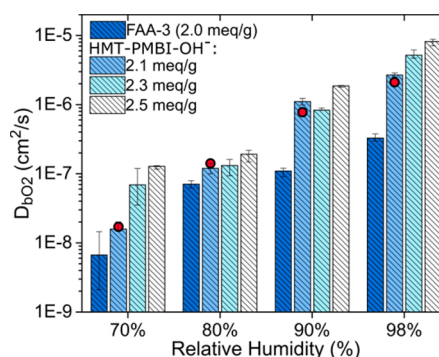
squares fits of the Shoup−Szabo equation to the current transients. 2D contour plots of the relative errors, where the diffusion coefficient and solubility coefficients are the y- and x-axis, respectively, have been previously reported and are used to indicate graphically the range of solutions to the Shoup−Szabo equation with the lowest error.[33] Least-squares fitting of the averaged current transient resulted in a best fit exhibiting 0.66% error, shown as the red point in Figure 6, whereas the green domain corresponds to Shoup−Szabo equation fits with an error less than the NRMSD of the averaged sets (i.e., <1.2% for the case of Figure 6). Other ionomer films yielded similar contour plots and error percentages (i.e., approximately 1% error).

$$NRMSD = \frac{\sqrt{\sum_{i=1}^{m} \frac{(I_{exp,i} - I_{avg,i})^2}{m}}}{\max(I_{exp}) - \min(I_{exp})} \qquad (3)$$

Calculated oxygen diffusion coefficients obtained from least-squares fitting are shown in Figure 7, where the best fitting error is generally <1%. In both the HMT-PMBI-OH⁻ series and FAA-3 ionomers, at any specific relative humidity, D_{bO2}
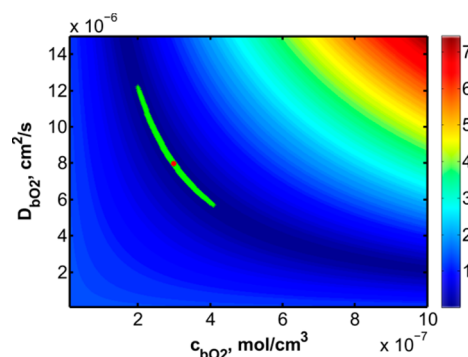

Figure 6. Contour plot for solutions of the Shoup−Szabo equation for 2.5 mequiv/g HMT-PMBI-OH⁻ at 98% RH and 60 °C. The color corresponds to % error, with the solution of minimum error being the red point and points that lie within experimental error represented by green points.

Figure 7. Oxygen diffusion coefficients obtained for HMT-PMBI-OH⁻ ionomer films and FAA-3 membranes by least-squares fitting of the Shoup−Szabo equation versus RH, 60 °C in air. The red points indicate values obtained for HMT-PMBI-OH⁻ 2.1 mequiv/g from numerical modeling (see text). Error bars correspond to the range of solutions for the mass transport limited current transients fit to the Shoup−Szabo equation.

displays a downward trend with decreasing IEC. This is because oxygen diffusion is correlated to the water content; where water content is proportional to the IEC within a similar family of polymer. For a given IEC, as RH is lowered there is a corresponding decrease in the oxygen diffusion coefficient. For example, the oxygen diffusion coefficient decreased by a factor of 170, 75, and 64 for the HMT-PMBI-OH⁻ series exhibiting 2.1, 2.3, and 2.5 mequiv/g IEC when the RH was decreased from 98% to 70%. The magnitude of the change in D_{bO2} for HMT-PMBI-OH⁻ films indicates that the higher the IEC, the less sensitive changes in RH are compared to lower IEC films. By comparison, FAA-3 membrane (IEC 2.0 mmol/g), decreased by a factor of 49 as RH was lowered from 98% to 70%.
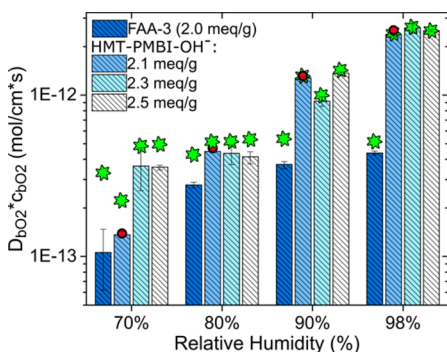
Oxygen solubility coefficients determined by chronoamperometry are shown in Figure 8, where oxygen solubility is observed to decrease with increasing IEC at a specific RH. Given that molecular oxygen predominantly prefers to dissolve in hydrophobic domains the findings are consistent with the highest c_{bO2} value being observed for polymers with the lowest water content, which occurs under conditions of lowest RH and polymers with the lowest IEC. For example, the oxygen concentration increases by a factor of 10 for HMT-PMBI-OH⁻ 2.1, 2.3, and 2.5 mequiv/g IEC when the RH is reduced from
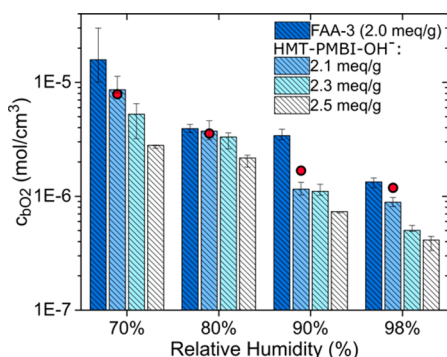
Figure 8. Oxygen solubility coefficients obtained for HMT-PMBI-OH⁻ ionomer films and FAA-3 membranes by least-squares fitting of the Shoup−Szabo equation versus RH, 60 °C in air. The red points indicate values obtained for HMT-PMBI-OH⁻ 2.1 mequiv/g from numerical modeling. Error bars correspond to the range of solutions for the mass transport limited current transients fit to the Shoup−Szabo equation.

98% to 70%. For FAA-3, the oxygen concentration increases by a factor of 12 upon decreasing RH from 98% to 70%.

Oxygen permeability coefficients, $D_{bO2}\cdot c_{bO2}$, obtained from the product of oxygen diffusion coefficient and solubility are shown in Figure 9. Also plotted, as a green star, is the oxygen

Figure 9. Oxygen permeability coefficients obtained for HMT-PMBI-OH⁻ ionomer films and FAA-3 membranes by least-squares fitting of the Shoup−Szabo equation versus RH, 60 °C in air. Green stars represent permeability coefficients determined from steady-state current, whereas red points indicate values obtained for HMT-PMBI-OH⁻ 2.1 mequiv/g from numerical modeling. Error bars correspond to the range of solutions for the mass transport limited current transients fit to the Shoup−Szabo equation.

permeability calculated from the pseudo-steady-state current, I_{SS}, obtained at $t = 5$ s in the current transient (e.g., see Figure 5) using eq 4:

$$I_{SS} = -4nFrD_{bO2}c_{bO2} \qquad (4)$$

where n is equal to 4, F is 96 485 C/mol, and r (cm) is the radius of the electrode (calculated from the effective electrode surface area). The permeability coefficients obtained from I_{SS} are generally larger than those obtained from curve fitting, with oxygen permeability coefficients being within 12% of the curve fit values at 98% RH, or as high as 100% in variation at lower RH, e.g., 70% RH. The variation in permeability coefficients obtained through fitting the Shoup−Szabo equation and extracted from I_{SS} can be explained by the fact that the latter method only uses one data point, and is not at a true steady state, whereas the former technique incorporates contributions from short, intermediate, and long times after stepping to ORR potentials. Within the HMT-PMBI-OH⁻ series at a specific IEC, the permeability coefficient is observed to decrease with decreasing RH. At a specific RH, as in investigations with hydrocarbon proton exchange membranes of varying IEC, there is no definitive trend.[20] Comparing the extent with which the oxygen diffusion coefficient decreases to that with which the oxygen solubility increases (see Figures 7 and 8), oxygen diffusion is the dominant factor that causes the oxygen permeability to decrease as RH is lowered. The oxygen permeability decreases by a factor of 4 for FAA-3; and 17, 7, and 7, for HMT-PMBI-OH⁻ 2.1, 2.3, and 2.5 mequiv/g IEC, respectively, upon decreasing the RH from 98 to 70%.

The HMT-PMBI-OH⁻ 2.5 mequiv/g film displays almost 5 times higher oxygen permeability at 90% RH, but half the oxygen permeability at 70% RH, compared to our previous reports of ORR mass transport in perfluorinated PEM polymers, namely Nafion 211.[25] Further comparison reveals that FAA-3 exhibits a slightly higher oxygen permeability at 90% RH compared to Nafion 211 but half the permeability at 70% RH.[25] Because the oxygen diffusion coefficient plays a dominant role in oxygen permeability, the high IEC and thus high water content in these hydrocarbon films explains the higher oxygen permeability for alkaline membranes at high RH.

A 28 μm thick Tokuyama A201 quaternized ammonium anion exchange membrane (IEC 1.8 mequiv/g) is reported to exhibit a D_{bO2} of 4.29×10^{-6} cm²/s under full hydration, 1 atm oxygen, at 20 °C. c_{bO2} is reported to be 0.93×10^{-6} mol/cm³, and the product, $D_{bO2}\cdot c_{bO2}$, 3.99×10^{-12} mol/(cm·s).[14] Oxygen mass transport coefficients of similar magnitude were reported for a 5 μm thick Tokuyama AS-4 ionomer film in 0.1 M KOH.[13] At 98% RH, and for a comparable IEC (2.1 mequiv/g), we report D_{bO2}, 2.7×10^{-6} cm²/s; c_{bO2}, 0.89×10^{-6} mol/cm³; and $D_{bO2}\cdot c_{bO2}$, 2.4×10^{-12} mol/(cm·s). Comparison of oxygen mass transport coefficients reported here as well as previously, for Nafion 211, are presented for two similar values of relative humidity in Table 1.

Table 1. Oxygen Mass Transport Coefficients Obtained through Nonlinear Curve Fitting of the Experimental Data with the Shoup−Szabo Equation

Ionomer	RH	D_{bO2} (cm²/s) ×10⁷	c_{bO2} (mol/cm³) ×10⁶	$D_{bO2}\cdot c_{bO2}$ (mol/(cm·s)) ×10¹²
HMT-PMBI-OH⁻ (2.1 mequiv/g)[a]	70%	0.16 ± 0.05	8.6 ± 3	0.14 ± 0.01
	90%	11 ± 2	1.2 ± 0.2	1.3 ± 0.03
FAA-3 (2.0 mequiv/g)[a]	70%	0.067 ± 0.08	15 ± 10	0.11 ± 0.05
	90%	0.11 ± 0.2	3.4 ± 0.5	0.37 ± 0.02
Nafion 211 (0.91 mequiv/g) from ref 25	70%	0.68	3.7	0.25
	90%	0.77	3.5	0.27

[a]This work.

Table 2. Comparison of Numerical and Analytical Results for 2.1 mequiv/g IEC HMT-PMBI-OH⁻ at 60 °C

RH, %	Exp. NRMSD (%)	Num. NRMSD (%)	c_{bO2}^{num} (mol/cm³)	D_{bO2}^{num} (cm²/s)	$D_{bO2} \cdot c_{bO2}$ (mol/(cm·s))	t_{trunc} (s)	t_{shift} (s)
70	0.71	0.95	7.950×10^{-6}	1.850×10^{-8}	1.471×10^{-13}	0.165	0.150
Difference from analytical fit, %			8.6	14.6	7.5	0.01	0.43
80	0.37	0.53	3.600×10^{-6}	1.408×10^{-7}	5.069×10^{-13}	0.162	0.138
Difference from analytical fit, %			3.8	14.9	11.7	3.04	1.35
90	0.53	0.69	1.588×10^{-6}	8.700×10^{-7}	1.382×10^{-12}	0.165	0.140
Difference from analytical fit, %			27.2	26.9	7.6	13.4	10.1
98	0.73	1.08	1.240×10^{-6}	2.110×10^{-6}	2.616×10^{-12}	0.179	0.162
Difference from analytical fit, %			28.5	27.0	9.0	17.9	12.2

The discrepancy between mass transport coefficients reported here and by those observed previously can be explained by the use of (a) different polymer materials and (b) different analytical models for parameter estimation. Gunasekara uses the Cottrell equation in the form that represents the first two terms in the short-time expansion by Aoki and Osteryoung and thus is subject to the restraint, $\frac{4D_{bO2}t}{r^2} < 1$.[34] For the reported electrode radius of 50 μm and 20 s duration of the experiment, the applicability range of the Cottrell equation is limited to D_{bO2} values of $<3.125 \times 10^{-7}$ cm²/s, which is much smaller than the fitted value of 4.29×10^{-6}, and may be out of the range of validity of the analytical model.

Comparing the values in Table 1, the oxygen diffusion coefficient for HMT-PMBI-OH⁻ 2.1 mequiv/g decreases 70 times more than Nafion 211 under similar conditions. The presented chronoamperometric measurements suggest a very strong dependence of oxygen diffusion on water content for HMT-PMBI-OH⁻, which is consistent with the report by Khadke et al. on Tokuyama AS-4 ionomer films, in which it was suggested that ORR mass transport limitations result from a lack of reactant water, rather than the availability of oxygen.[15]

For comparative purposes, values for D_{bO2}, c_{bO2}, and $D_{bO2} \cdot c_{bO2}$ for all samples calculated using the geometric radius of the working electrode (5 μm) in the Shoup–Szabo equation, rather than the effective radius, are shown in Figures S5–S7. The stark difference between approaches can be seen in the solubility coefficient comparison (Figure S6), where oxygen concentration is found to increase with decreasing IEC when using the geometric radius, which is counter to every trend observed in the literature where the higher water content afforded by higher IEC should cause oxygen solubility to decrease.[20] In contrast, using the effective radius to determine oxygen concentration provides the expected, logical trend of decreasing oxygen concentration with increasing IEC/water content.

Numerical Modeling. The results reported above were obtained using the Shoup–Szabo equation (eq 2). A critical assumption made in utilizing this equation is that the ionomer is infinitely thick and hence the oxygen depletion region does not reach the surface of the film during the lifetime of the experiment.[26] It is also recognized that the Shoup–Szabo equation has a limited power of approximation of the radial diffusion, which are given by the second and subsequent terms of the short- and long-time expansions of the equation obtained by Aoki and Osteryoung.[26,34] To examine the applicability of the Shoup–Szabo equation for these particular ionomer films, under these particular conditions, an axisymmetric, two-dimensional numerical model of the diffusion process in cylindrical coordinates was developed and solved in the open source Fuel Cell Simulation Toolbox (OpenFCST).[35] Fuller

details of the model are provided in the Supporting Information.

Numerical modeling was performed for the HMT-PMBI-OH⁻ 2.1 mequiv/g IEC ionomer. As can be seen from Table S1, the diffusion length, L_D, estimated by eq 5:

$$L_D = 2\sqrt{5D_{bO2}^{an}} \tag{5}$$

is much smaller than the thickness of the ionomer in the 70% RH case for the experimental time interval of 5 s. The diffusion length is close to the film thickness when the RH is 90% RH, and it is well beyond the film thickness at 98% RH, where the water content of the film and the corresponding diffusion coefficients are much larger. It is surmised that the analytically obtained results (using the Shoup–Szabo equation) are less valid in the latter two cases. Using the numerical simulation, we were able to estimate the errors associated with the assumptions made in deriving the Shoup–Szabo model (see below).

Numerically obtained oxygen transport properties are shown in Table 2, and the values for D_{bO2}, c_{bO2}, and $D_{bO2} \cdot c_{bO2}$ are plotted in Figures 7–9 as red points in order to compare them visually to analytically obtained values. Contour plots showing the associated NRMSD, including the solutions with minimum error, obtained from applying the numerical model on the current transients for 70% to 98% RH can be seen in Figure 10. The magnitude of change in D_{bO2}, c_{bO2}, and $D_{bO2} \cdot c_{bO2}$ observed as RH decreases for 2.1 mequiv/g HMT-PMBI-OH⁻ relates well to the analytically obtained results. Specifically, D_{bO2} decreased by 114 times (compared to 170, analytically) whereas $D_{bO2} \cdot c_{bO2}$ decreased by 18 times (compared to 17, analytically) when the RH was lowered from 98% to 70%, and c_{bO2} increased by 6 times (compared to 10, analytically). Results for the 80% RH case were the closest to analytically fitted values, exhibiting only a 3.8% difference in oxygen solubility and a 14.9% difference in oxygen diffusion coefficient. As the oxygen diffusion coefficient increases with increasing RH (and thus water content), the gas distribution in the domain is increasingly affected by its encroachment on the film's physical boundary, making conventional analytical models, such as Cottrell and Shoup–Szabo analyses, less accurate. The difference between the numerical and analytical solution, computed with respect to the numerical results, was 27.2% and 28.5% with respect to oxygen solubility at 90% and 98% RH, respectively; and 26.9% and 27.0%, respectively, for diffusivity. The product of oxygen solubility and oxygen diffusion coefficient, i.e., permeability, was found to be reasonably accurate (<12% error) in all cases. The Shoup–Szabo equation fits obtained analytically were quite reasonable, with an NRMSD from experimental data of 0.53–0.73%; however, the Shoup–Szabo equation introduces a significant error in the computation of D_{bO2} and c_{bO2} independently due to
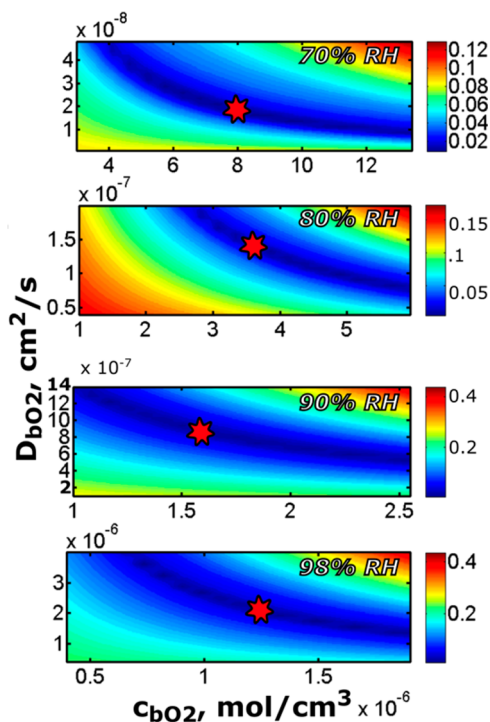
Figure 10. Contour plots for numerical fit normalized root-mean-square deviation (NRMSD) for 2.1 mequiv/g HMT-PMBI-OH⁻ at 60 °C. Color corresponds to % NRMSD, whereas the red stars correspond to minimum % NRMSD.

the fact that the simplifying assumptions are not valid when the oxygen diffusion length reaches the film thickness during the experimental time scale. As an example, Figure 11 shows the
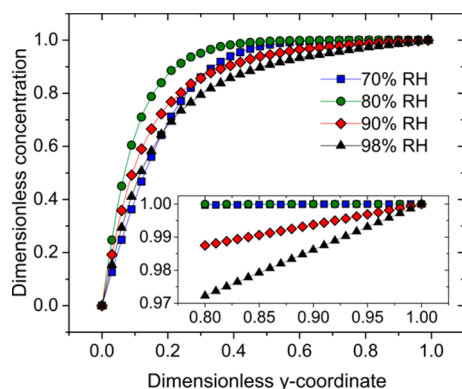
Figure 11. Dimensionless oxygen concentration (where a value of 1 represents bulk oxygen) distribution under the center of the electrode ($x-0$) versus dimensionless y-coordinate (film thickness normalized to gas−ionomer boundary) for 2.1 mequiv/g HMT-PMBI-OH⁻ for 70%, 90%, and 98% RH at 60 °C, $t \cong 5$ s. Inset: zoom showing slopes present at 90% and 98% RH, which indicate oxygen flux at gas−ionomer boundary.

dimensionless distribution of oxygen concentration along dimensionless axis, $x = 0$, (coinciding with the central axis of the electrode or the axis of symmetry of the computational domain) at $t \cong 5$ s for different RH conditions. Coordinate $y = 1$ represents the gas−ionomer interface, and a nonzero slope of concentration around that point at 90% and 98% RH indicates the presence of a nonzero flux of oxygen diffusing into the domain. This effect is not taken into account by any

conventional analytical model, be it the Cottrell or the Shoup−Szabo equation. It is also worth noting that the analytical relation used to estimate diffusion length in Table S1 given by eq 5[28] does not provide sufficient insight into actual diffusion propagation as it clearly underestimates it. Therefore, when possible, the numerical model is recommended over the analytical approximations for the purpose of fitting the gas transport properties in ionomers in order to obtain accurate results. Moreover, the numerical model may have multidisciplinary applicability for electrochemical measurements in systems using thin materials where an interfacial boundary is present, such as reactant mass transport through biological films.[36,37]

CONCLUSIONS

A novel anion exchange ionomer as well as a commercially available AAEM membrane of comparative thickness were investigated for ORR transport parameters using a 2-electrode solid-state microelectrode electrochemical cell. It was discovered that the effective surface area of the working electrode decreased as relative humidity was reduced. The effective surface area was also lower for lower IEC membranes. In contrast, although FAA-3 possesses a lower IEC than the HMT-PMBI-OH⁻ films analyzed, a higher overall effective working electrode area was observed. All three effects correlated to the films water content. The effective surface areas approached that in aqueous KOH under conditions of high RH.

Oxygen mass transport parameters were calculated using least-squares fitting of the Shoup−Szabo equation, where the oxygen diffusion coefficient was observed to decrease for all ionomer films as relative humidity and/or ion exchange capacity were reduced. The oxygen solubility, on the other hand, was observed to increase as either ion exchange capacity or relative humidity were reduced. The oxygen permeability coefficient decreased by over 1 order of magnitude when subjected to less than a 30% drop in RH at 60 °C.

The accuracy of the fits of the Shoup−Szabo equation for analyzing oxygen mass transport in thin ionomer films was investigated by numerical modeling, which showed parity for oxygen permeability coefficients (between 7% and 12% accuracy). For accurate D_{bO2} and c_{bO2} estimation, however, the numerical model is preferable over the Shoup−Szabo equation due to the simplifying assumptions needed to derive the model. The large decrease in D_{bO2} observed when RH is lowered, coupled with the large decrease in current response at 70% RH compared to higher humidities, reinforces a primary limiting factor in anion exchange ionomer design, that the hydration of the membrane limits mass transport of reactants in the cathode catalyst layer.

ASSOCIATED CONTENT

ⓢ Supporting Information

The Supporting Information is available free of charge via the Internet at The Supporting Information is available free of charge on the ACS Publications website at DOI: 10.1021/jacs.6b09217.

Experimental details, numerical modeling parameters, and data (PDF)

■ AUTHOR INFORMATION

Corresponding Author
*holdcrof@sfu.ca

Author Contributions
The paper was written through contributions of all authors. All authors have given approval to the final version of the paper.

■ REFERENCES

(1) Merle, G.; Wessling, M.; Nijmeijer, K. *J. Membr. Sci.* **2011**, *377* (1−2), 1−35.

(2) Antolini, E.; Gonzalez, E. R. *J. Power Sources* **2010**, *195* (11), 3431−3450.

(3) Markovic, N.; Gasteiger, H.; Ross, P. N.; Berkeley, L.; Division, M. S. *J. Electrochem. Soc.* **1997**, *144* (5), 1591−1597.

(4) Wang, J.; Wang, J.; Zhang, S. *J. Membr. Sci.* **2012**, *415−416*, 205−212.

(5) Noonan, K. J. T.; Hugar, K. M.; Kostalik, H. a; Lobkovsky, E. B.; Abruña, H. D.; Coates, G. W. *J. Am. Chem. Soc.* **2012**, *134* (44), 18161−18164.

(6) Faraj, M.; Elia, E.; Boccia, M.; Filpi, A.; Pucci, A.; Ciardelli, F. *J. Polym. Sci., Part A: Polym. Chem.* **2011**, *49* (15), 3437−3447.

(7) Chen, D.; Hickner, M. A. *ACS Appl. Mater. Interfaces* **2012**, *4* (11), 5775−5781.

(8) Henkensmeier, D.; Kim, H.-J.; Lee, H.-J.; Lee, D. H.; Oh, I.-H.; Hong, S.-A.; Nam, S.-W.; Lim, T.-H. *Macromol. Mater. Eng.* **2011**, *296* (10), 899−908.

(9) Thomas, O. D.; Soo, K. J. W. Y.; Peckham, T. J.; Kulkarni, M. P.; Holdcroft, S. *Polym. Chem.* **2011**, *2* (8), 1641−1643.

(10) Wright, A. G.; Fan, J.; Britton, B.; Weissbach, T.; Lee, H.-F.; Kitching, E. A.; Peckham, T. J.; Holdcroft, S. *Energy Environ. Sci.* **2016**, *9* (6), 2130−2142.

(11) Wright, A. G.; Holdcroft, S. *ACS Macro Lett.* **2014**, *3* (5), 444−447.

(12) Wright, A. G.; Weissbach, T.; Holdcroft, S. *Angew. Chem., Int. Ed.* **2016**, *55* (15), 4818−4821.

(13) Khadke, P. S.; Krewer, U. *J. Phys. Chem. C* **2014**, *118* (21), 11215−11223.

(14) Gunasekara, I.; Lee, M.; Abbott, D.; Mukerjee, S. *ECS Electrochem. Lett.* **2012**, *1* (2), F16−F19.

(15) Khadke, P. S.; Krewer, U. *Electrochem. Commun.* **2015**, *51*, 117−120.

(16) Parthasarathy, A.; Srinivasan, S.; Appleby, A. J. *J. Electrochem. Soc.* **1992**, *139* (9), 2530−2537.

(17) Parthasarathy, A.; Srinivasan, S.; Appleby, A. J. *J. Electrochem. Soc.* **1992**, *139* (10), 2856−2862.

(18) Basura, V.; Beattie, P.; Holdcroft, S. *J. Electroanal. Chem.* **1998**, *458* (1−2), 1−5.

(19) Beattie, P. D.; Basura, V. I.; Holdcroft, S. *J. Electroanal. Chem.* **1999**, *468* (2), 180−192.

(20) Basura, V. I.; Chuy, C.; Beattie, P. D.; Holdcroft, S. *J. Electroanal. Chem.* **2001**, *501* (1−2), 77−88.

(21) Chlistunoff, J.; Uribe, F.; Pivovar, B. *ECS Trans.* **2006**, *1*, 137−146.

(22) Chlistunoff, J. *J. Power Sources* **2014**, *245*, 203−207.

(23) Carmo, M.; Doubek, G.; Sekol, R. C.; Linardi, M.; Taylor, A. D. *J. Power Sources* **2013**, *230*, 169−175.

(24) Britton, B.; Holdcroft, S. *J. Electrochem. Soc.* **2016**, *163* (5), F353−F358.

(25) Novitski, D.; Holdcroft, S. *ACS Appl. Mater. Interfaces* **2015**, *7* (49), 27314−27323.

(26) Shoup, D.; Szabo, A. *J. Electroanal. Chem. Interfacial Electrochem.* **1982**, *140* (2), 237−245.

(27) Basha, C. A.; Rajendran, L. *Int. J. Electrochem. Sci.* **2006**, *1* (6), 268−282.

(28) Bard, A. J.; Faulkner, L. R. *Electrochemical Methods: Fundamentals and Applications*; Wiley, 2000; Vol. 6.

(29) Ahuja, A. K.; Behrend, M. R.; Whalen, J. J.; Humayun, M. S.; Weiland, J. D. *IEEE Trans. Biomed. Eng.* **2008**, *55* (4), 1457−1460.

(30) Peron, J.; Mani, A.; Zhao, X.; Edwards, D.; Adachi, M.; Soboleva, T.; Shi, Z.; Xie, Z.; Navessin, T.; Holdcroft, S. *J. Membr. Sci.* **2010**, *356* (1−2), 44−51.

(31) Lindström, R. W.; Kortsdottir, K.; Wesselmark, M.; Oyarce, A.; Lagergren, C.; Lindbergh, G. *J. Electrochem. Soc.* **2010**, *157* (12), B1795−B1801.

(32) He, Q.; Kusoglu, A.; Lucas, I. T.; Clark, K.; Weber, A. Z.; Kostecki, R. *J. Phys. Chem. B* **2011**, *115* (40), 11650−11657.

(33) Xiong, L.; Aldous, L.; Henstridge, M. C.; Compton, R. G. *Anal. Methods* **2012**, *4* (2), 371−376.

(34) Aoki, K.; Osteryoung, J. *J. Electroanal. Chem. Interfacial Electrochem.* **1981**, *122*, 19−35.

(35) Secanell, M.; Putz, A.; Wardlaw, P.; Zingan, V.; Bhaiya, M.; Moore, M.; Zhou, J.; Balen, C.; Domican, K. *ECS Trans.* **2014**, *64* (3), 655−680.

(36) Macpherson, J. V.; O'Hare, D.; Unwin, P. R.; Winlove, C. P. *Biophys. J.* **1997**, *73* (5), 2771−2781.

(37) Buerk, D. G. *Methods Enzymol.* **2004**, *381*, 665−690.